

## Supporting Information

For

### **Amino-Tethered Ni<sub>3</sub>S<sub>2</sub>/MoS<sub>2</sub> Heterojunction for Coupling Electrochemical 5-Hydroxymethylfurfural Oxidation with 4-Nitrophenol Hydrogenation**

Tao Chen, Yulong Li, Fangpei Ma, Mingdong Sun, Ping Fu, Xiaoling Liu, Yu Zhou\*,  
and Jun Wang\*

State Key Laboratory of Materials-Oriented Chemical Engineering, College of

Chemical Engineering, Nanjing Tech University, Nanjing, 211816, China

#### **Corresponding Authors**

E-mail: njutzhouyu@njtech.edu.cn (Y. Zhou); junwang@njtech.edu.cn (J. Wang).

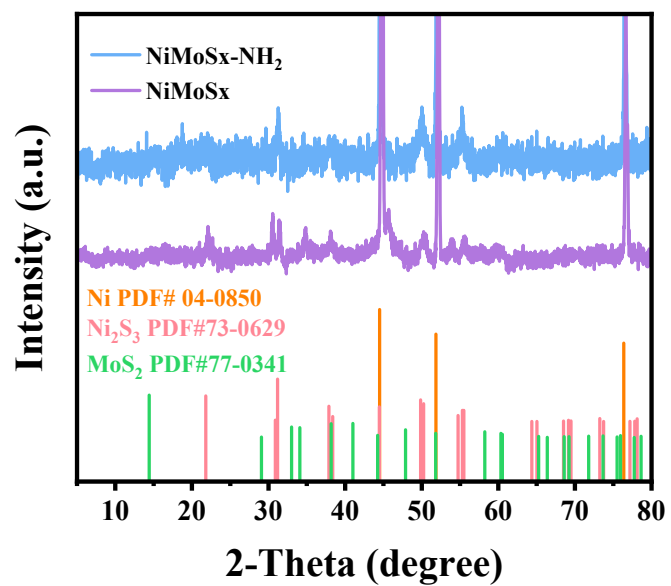


**Fig. S1.** XRD patterns of NiMoSx and NiMoSx-NH<sub>2</sub>.

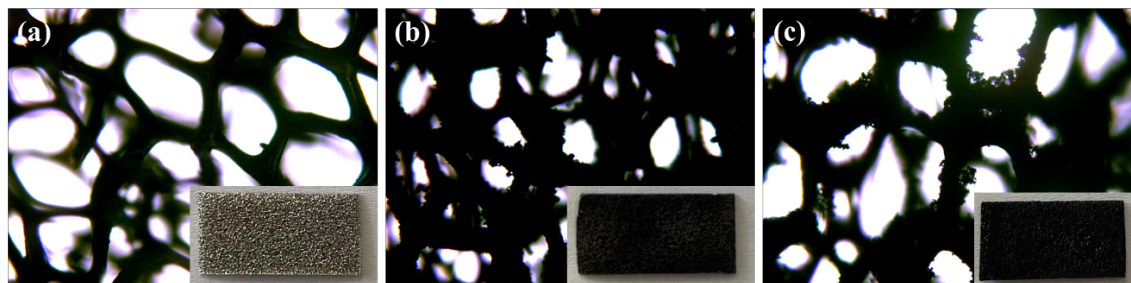


**Fig. S2.** Optical microscope images of (a) nickel foam, (b) NiMoSx, and (c) NiMoSx-NH<sub>2</sub>.

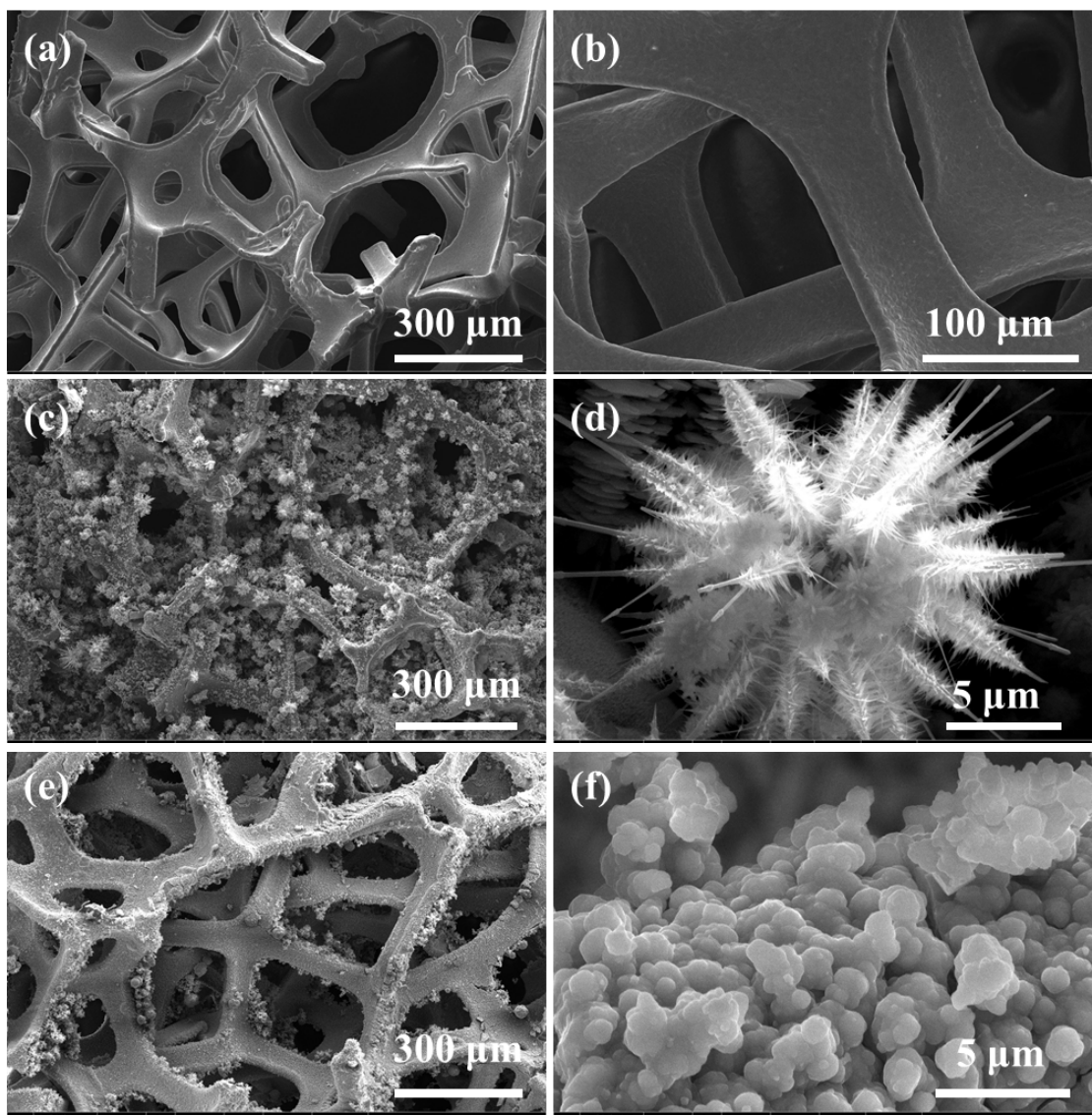


**Fig. S3.** SEM images of (a, b) nickel foam, (c, d) NiMoSx, and (e, f) NiMoSx-NH<sub>2</sub>.

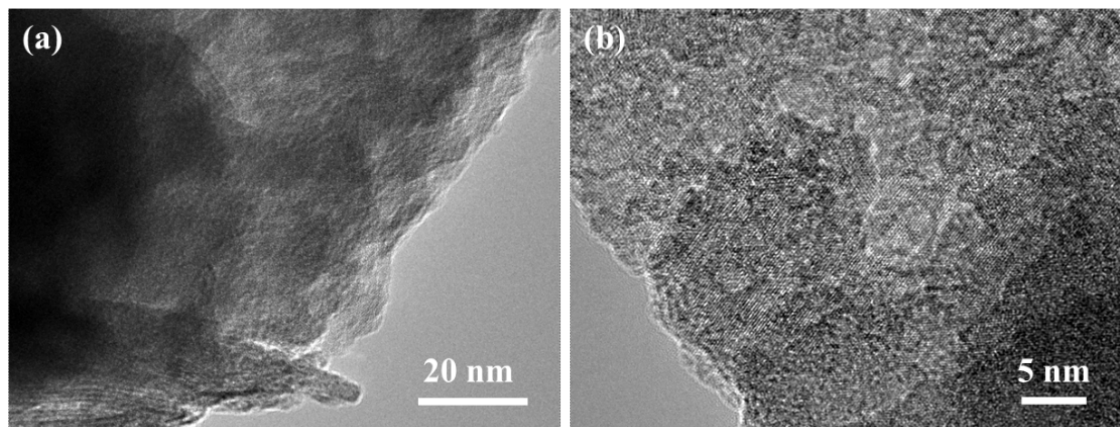


**Fig. S4.** TEM images of NiMoSx-NH<sub>2</sub>.

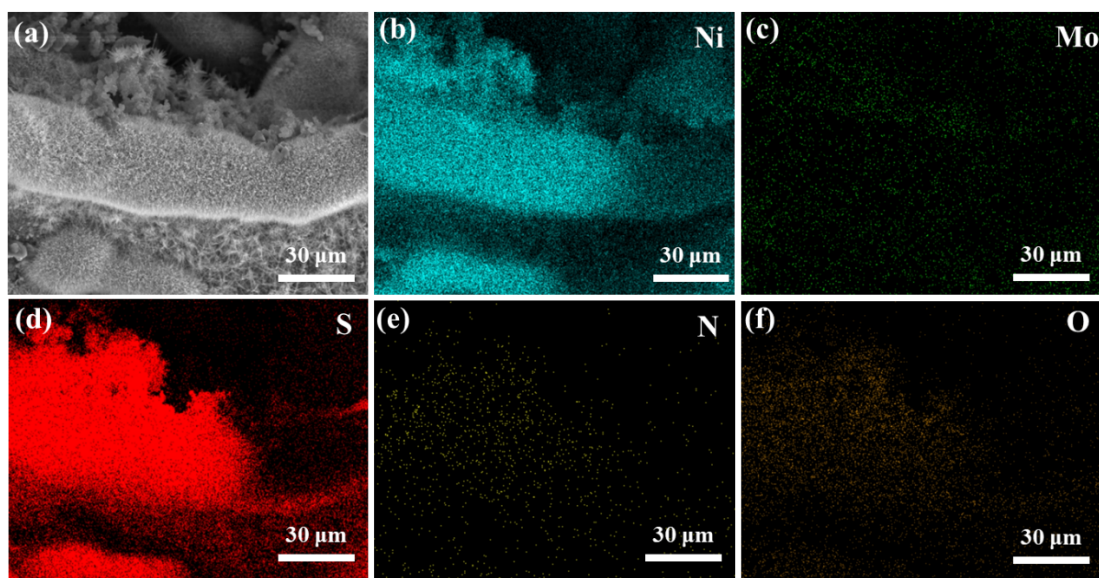


**Fig. S5.** Elemental mapping images showing the uniform distribution of (b) Ni, (c) Mo, (d) S, (e) N, and (f) O elements on NiMoSx.

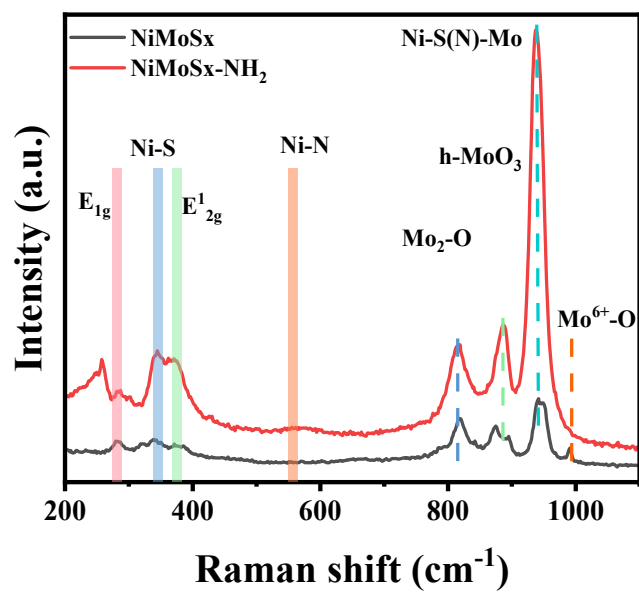


**Fig. S6.** Raman spectra of NiMoSx and NiMoSx-NH<sub>2</sub>.

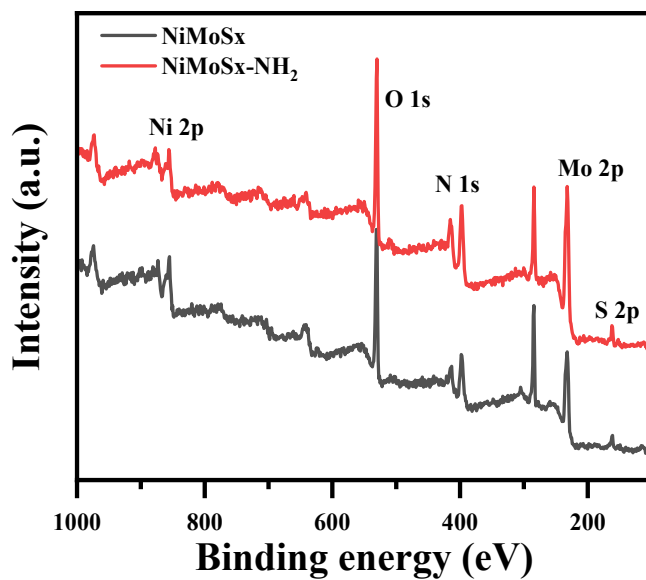


**Fig. S7.** Survey scan XPS spectra of NiMoSx and NiMoSx-NH<sub>2</sub>.

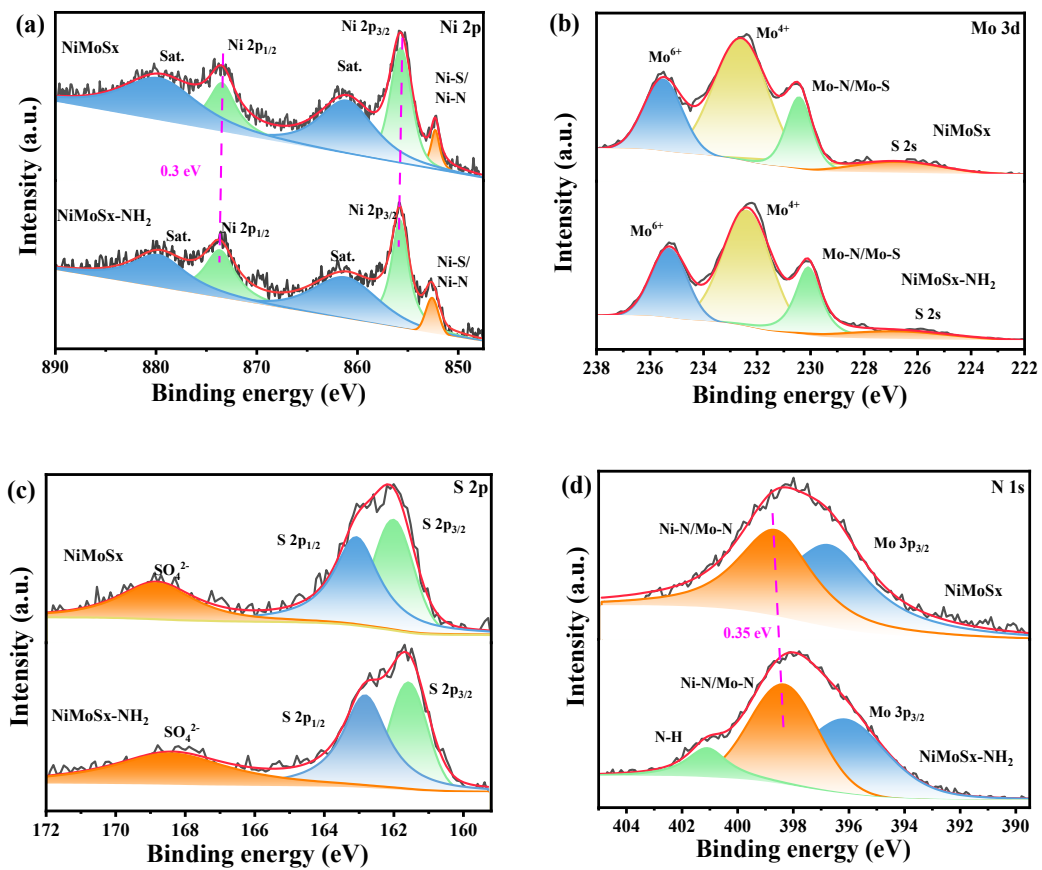


**Fig. S8.** High-resolution (a) Ni 2p, (b) Mo 3d, (c) S 2p, and (d) N 1s XPS spectra of NiMoSx and NiMoSx-NH<sub>2</sub>.

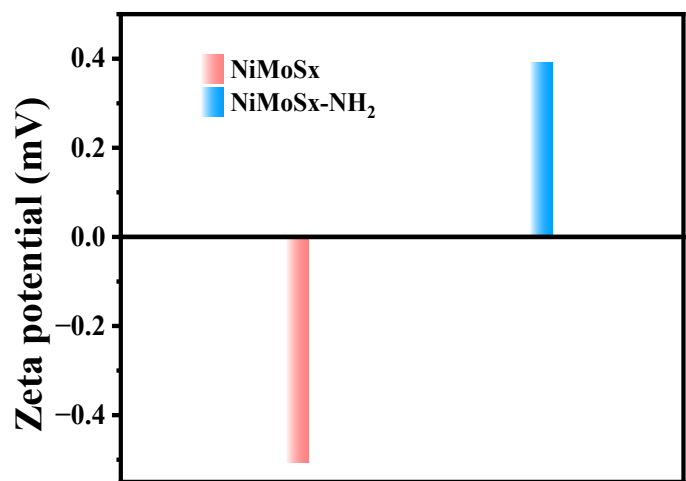


**Fig. S9.** Zeta potential measurements of NiMoSx and NiMoSx-NH<sub>2</sub>.

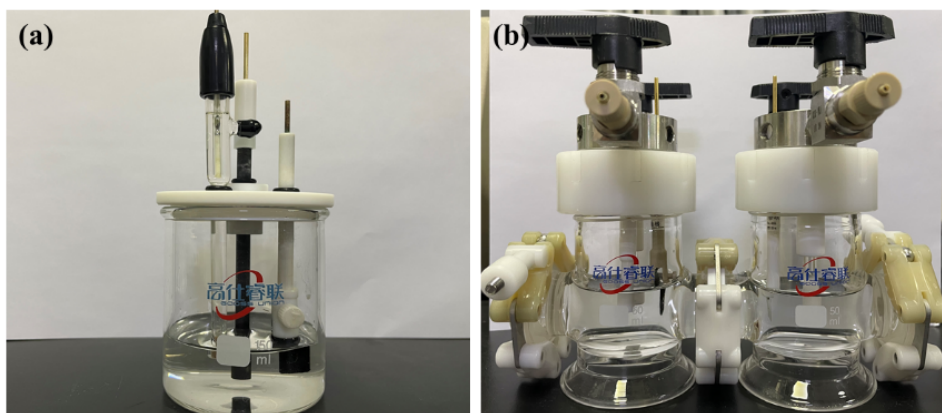


**Fig. S10.** The optical images of the related (a) undivided cell and (b) H-type divided cell reactors.

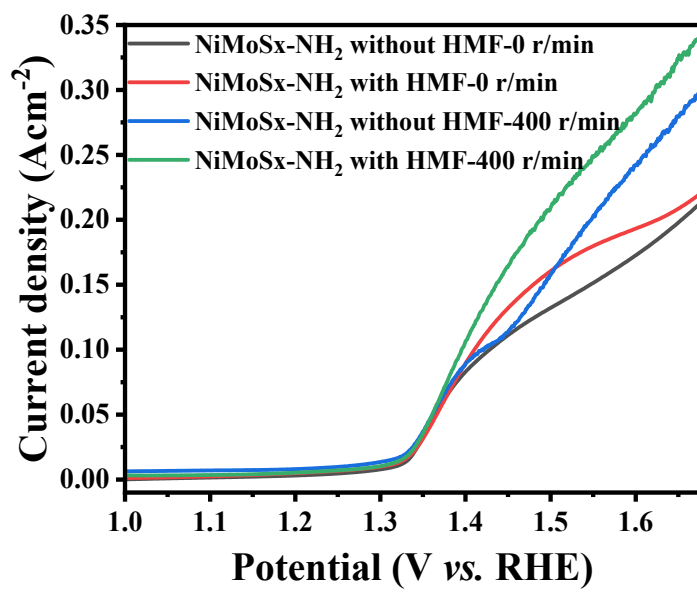


**Fig. S11.** LSV curves of NiMoSx-NH<sub>2</sub> in 1.0 M KOH aqueous solution with or without 10 mM HMF at different stirring speeds.

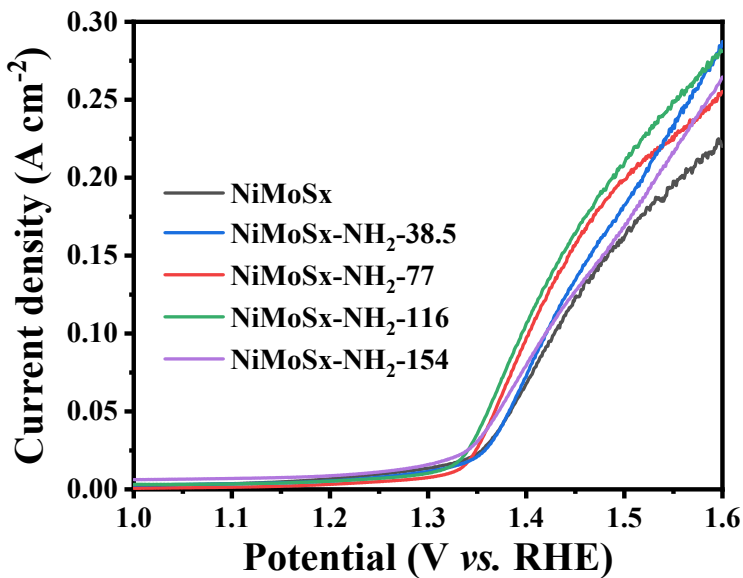


**Fig. S12.** LSV curves in 1 M KOH aqueous solution with 10 mM HMF of NiMoSx-NH<sub>2</sub>-*x* series (*x* is the amount of ammonia).

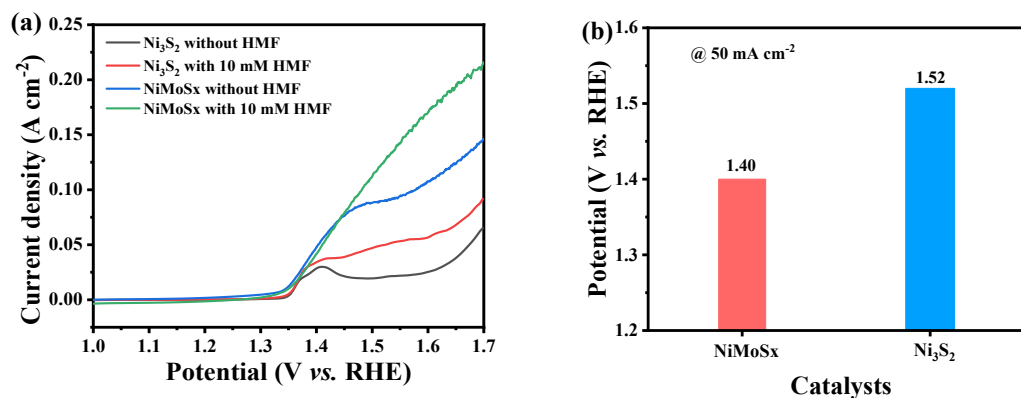


**Fig. S13.** (a) LSV curves, (b) potentials required at  $50 \text{ mA cm}^{-2}$  in 1.0 M KOH aqueous solution with 10 mM HMF of  $\text{Ni}_3\text{S}_2$  and NiMoSx.

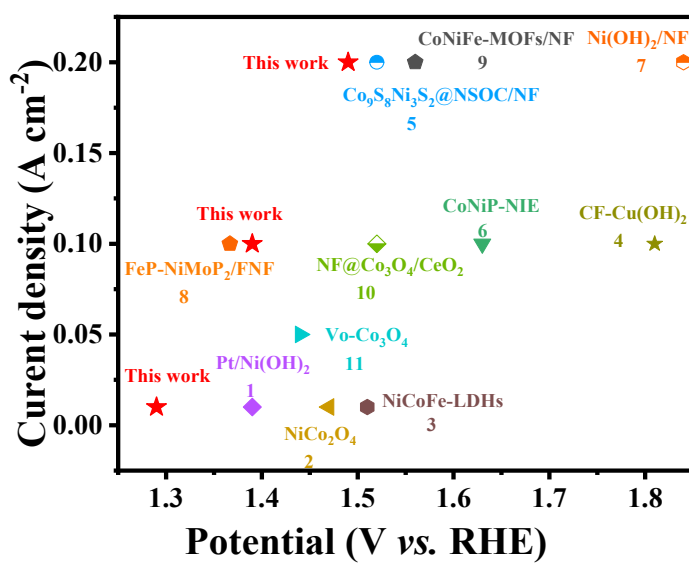


**Fig. S14.** Comparison of the performance of NiMoSx-NH<sub>2</sub> with previous state-of-the-art electrocatalysts.<sup>[1-11]</sup>

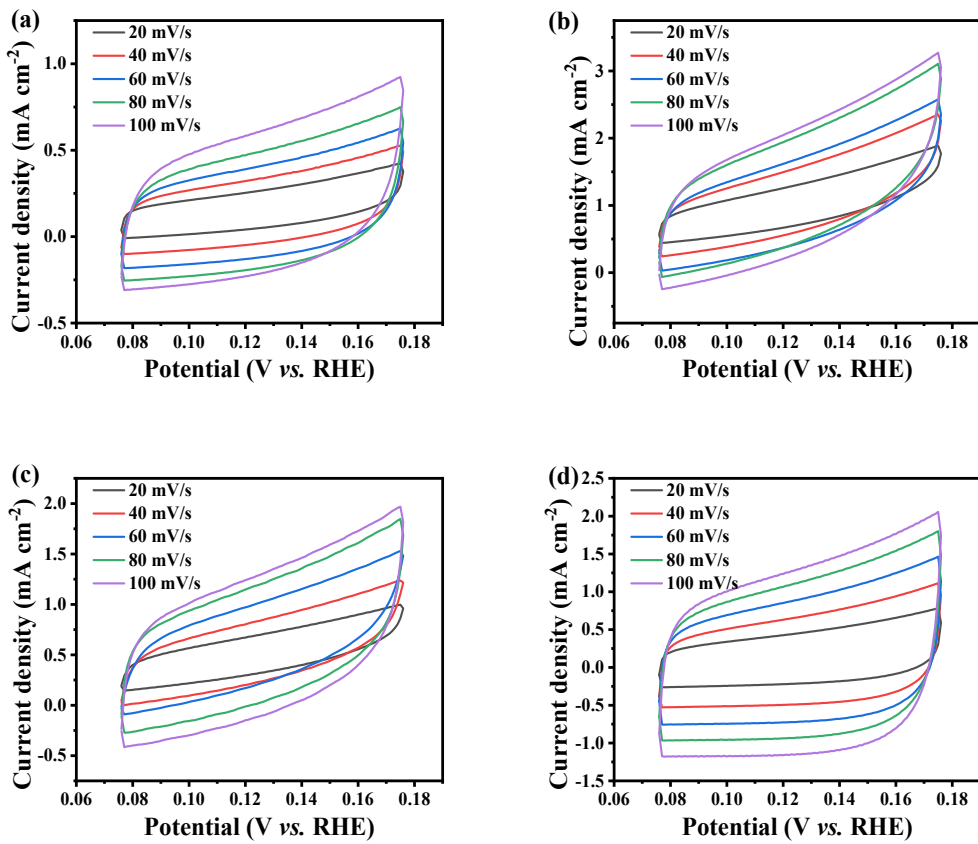


**Fig. S15.** CV curves of NiMoSx and NiMoSx-NH<sub>2</sub> in 1 M KOH aqueous solution without (a, c) or with (b, d) 10 mM HMF with the scan rate ranging from 20 mVs<sup>-1</sup> to 100 mVs<sup>-1</sup>.

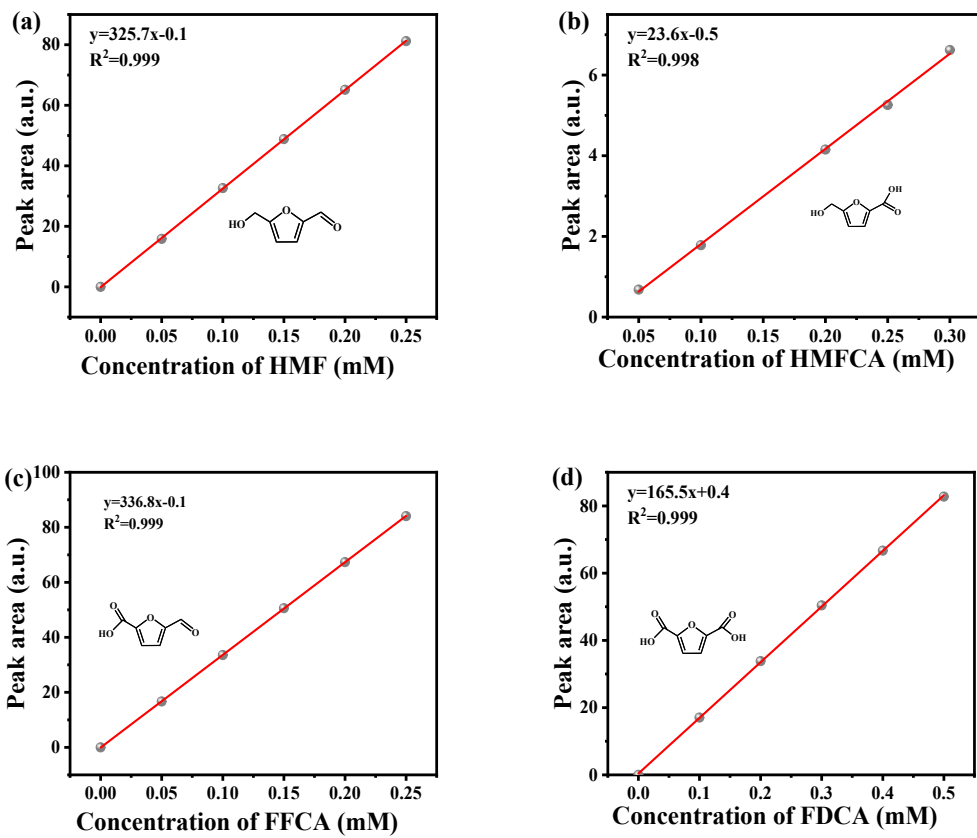


**Fig. S16.** The corresponding calibration curves for the quantitative analysis of (a) HMF, (b) HMFCA, (c) FFCA, and (d) FDCA.

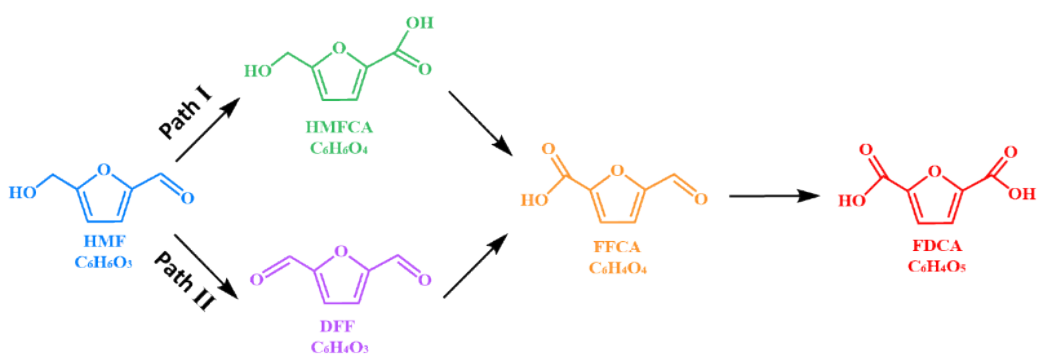


**Fig. S17.** The possible pathways for the HMF oxidation into FDCA.

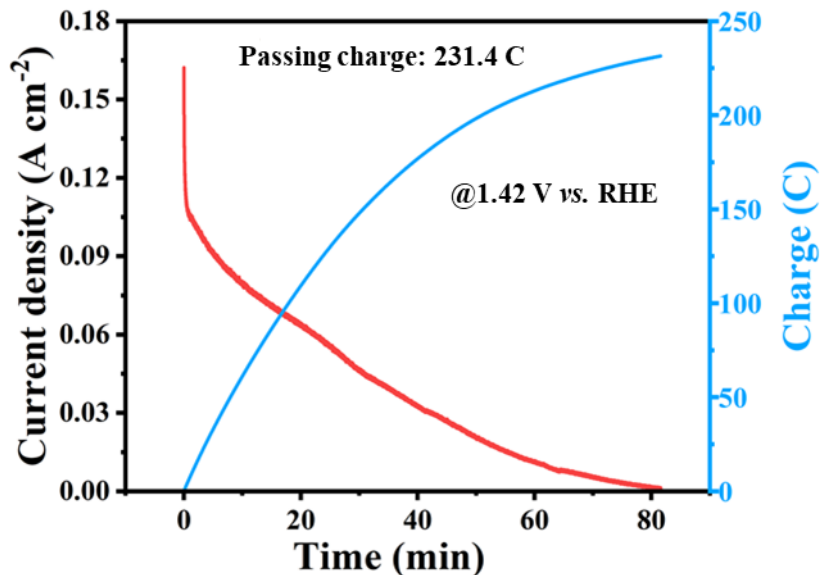


**Fig. S18.** The chronoamperometric response curve of NiMoSx-NH<sub>2</sub> in a 1.0 M KOH aqueous solution with 10 mM HMF.

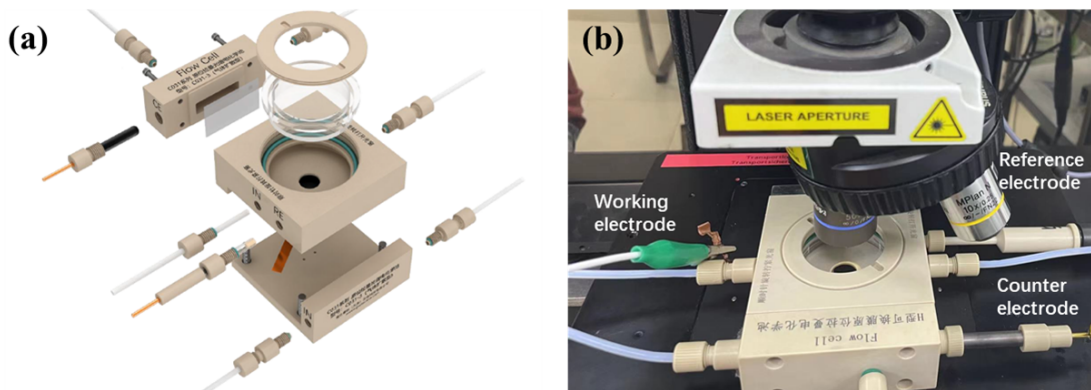


**Fig. S19.** (a) The electrolytic cell used for *in situ* Raman experiments and (b) a diagram of the device for the collection of Raman spectra.

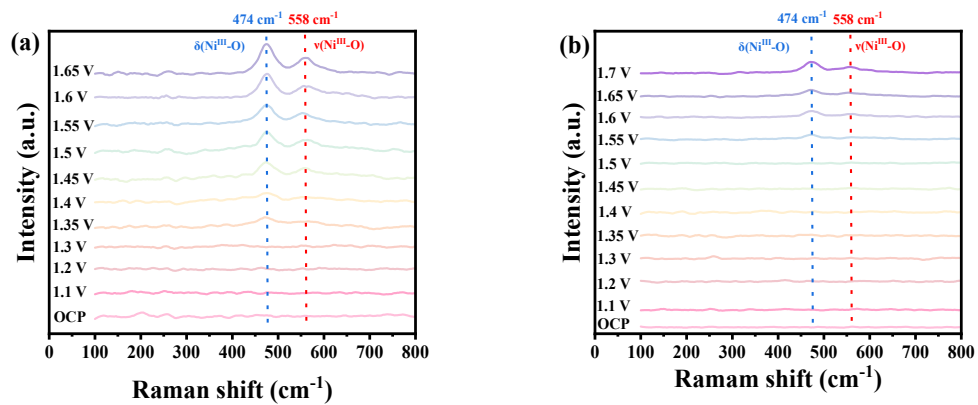


**Fig. S20.** *In situ* Raman spectra of NiMoSx-NH<sub>2</sub> in 1 M KOH solution (a) without or with 10 mM HMF.

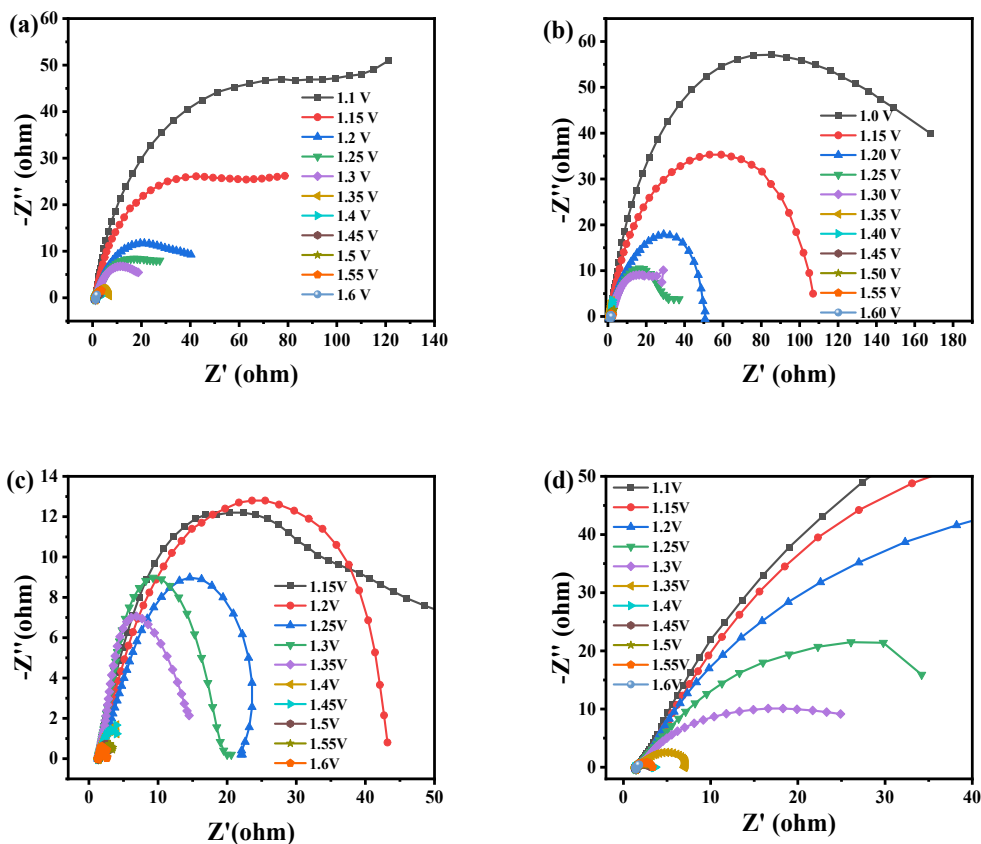


**Fig. S21.** *In situ* Nyquist plots of NiMoSx and NiMoSx-NH<sub>2</sub> in (a, c) 1 M KOH for OER, and (b, d) 1 M KOH with 50 mM HMF for HMFOR.

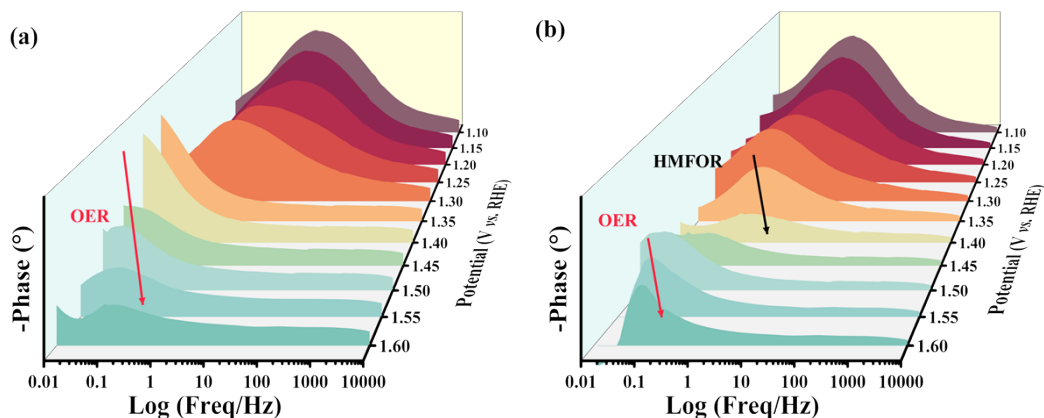


**Fig. S22.** Bode phase plots of the *in situ* EIS spectra of NiMoSx in (a) 1 M KOH, and (b) 1 M KOH with 50 mM HMF.

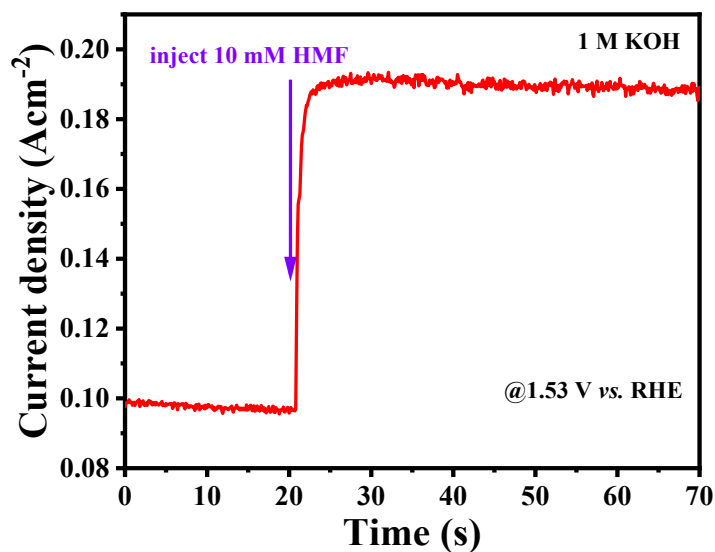


**Fig. S23.** The chronoamperometry curve of NiMoSx-NH<sub>2</sub> electrode in 1 M KOH at 1.53 V (vs. RHE).

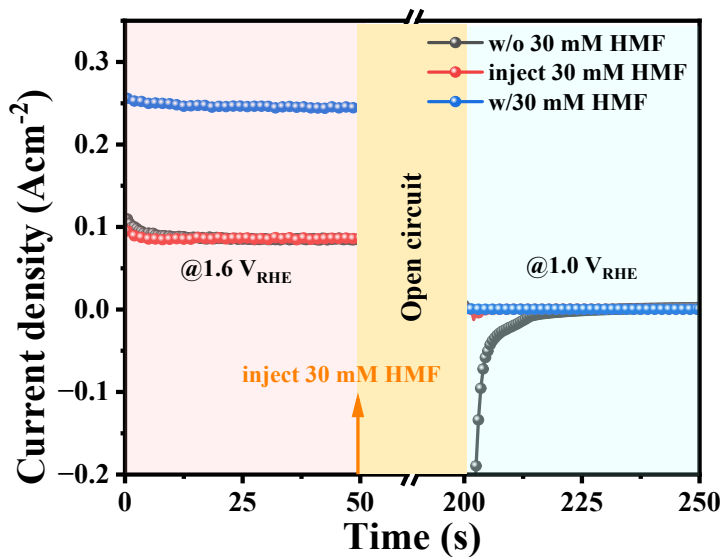


**Fig. S24.** Multi-potential step curves of NiMoSx in 1M KOH solutions without and with 30 mM HMF. In all panels, the pink, orange, and pale shaded areas indicate the application of a constant voltage of 1.60 V (vs. RHE), an open-circuit process and the application of an open circuit voltage of 1.00 V (vs. RHE), respectively.

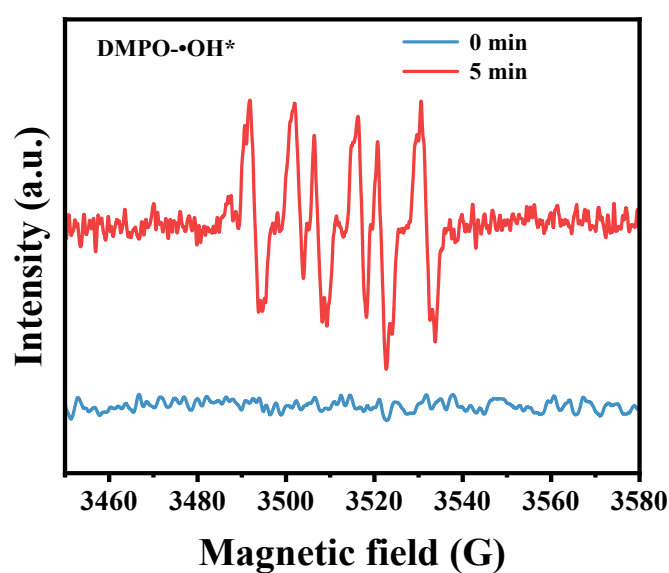


**Fig. S25.** Time-dependent ESR spectra of NiMoSx-NH<sub>2</sub> in the presence of DMPO in 1 M KOH aqueous solution with 10 mM HMF for HMFOR.

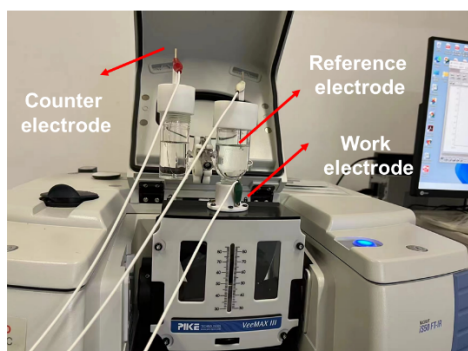


**Fig. S26.** The photograph of the electrolytic cell used in FTIR experiments.

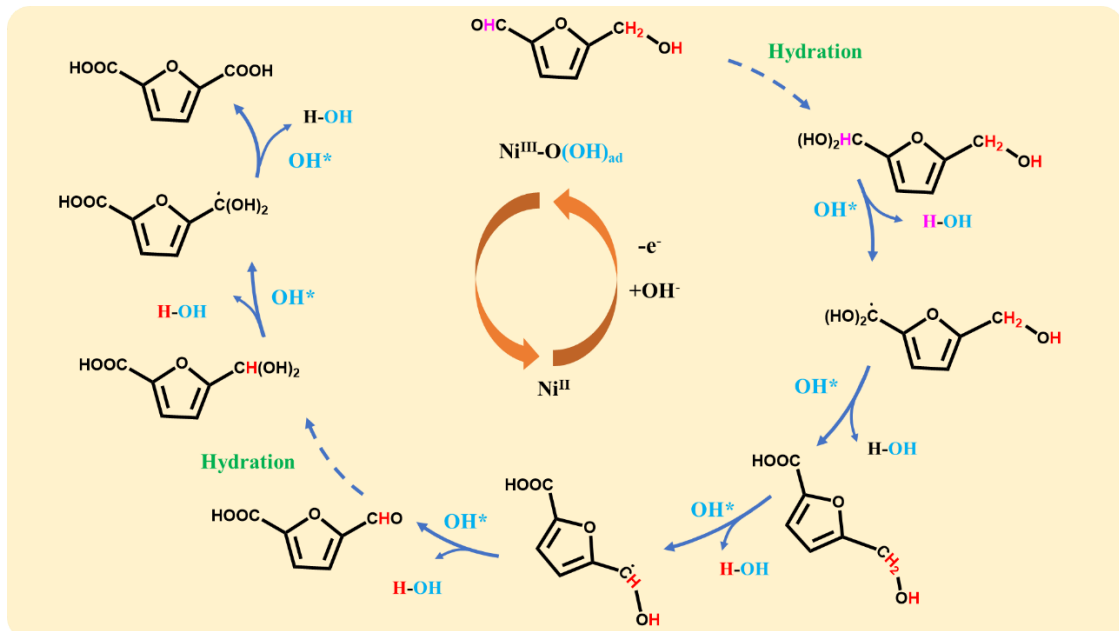


**Fig. S27.** The illustration of HMF oxidation reaction mechanism over the electrocatalyst.

**Note 1.** Based on the above results, we propose the reaction mechanism of the catalytic process as in **Fig. S27**. Based on the *in situ* Raman and previous work,<sup>[12]</sup> Ni<sup>II</sup> in the catalyst undergoes a proton-coupled electron transfer (PCET) process at the anode, forming Ni<sup>III</sup>-O(OH)<sub>ad</sub> as the active sites for electrocatalytic HMF oxidation. The aldehyde group of HMF undergoes hydration under strongly alkaline conditions to produce a gem-diol intermediate. The hydrogen atoms in the gem-diol intermediate reacted with the OH\* generated by Ni<sup>III</sup>-O(OH)<sub>ad</sub> rapidly to form HMFACA *via* a two-step dehydration process. Subsequently, the generated OH\* attacks the alcohol hydroxyl group and the nearby C–H bond to yield FFCA *via* a two-step dehydration process. Finally, the aldehyde group in FFCA undergoes the same process of hydration and dehydration process to form FDCA, completing the whole catalytic cycle. Surface amino modification benefits accelerate the formation of Ni<sup>III</sup> species to generate more active centers and promote HMF adsorption, resulting in excellent catalytic performance.

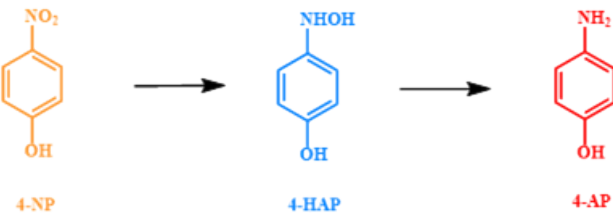


**Fig. S28.** The possible pathways for the electrocatalytic hydrogenation of 4-NP into 4-AP.

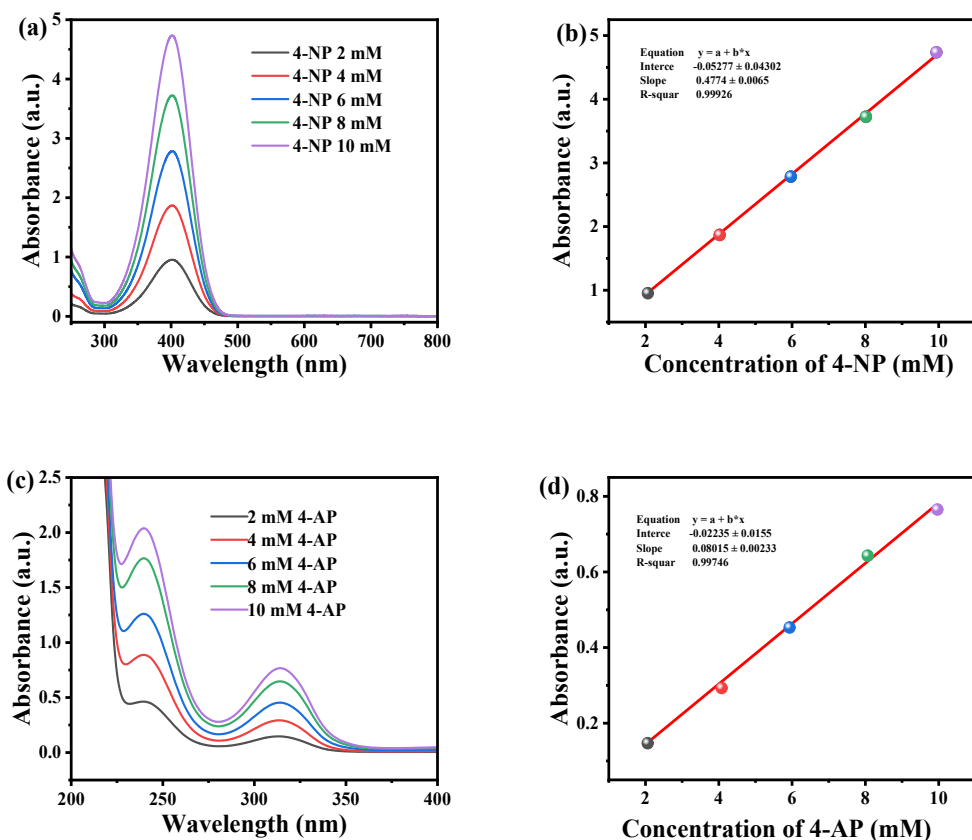


**Fig. S29.** UV-vis absorption spectra and calibration curves of (a, b) 4-NP and (c, d) 4-AP.

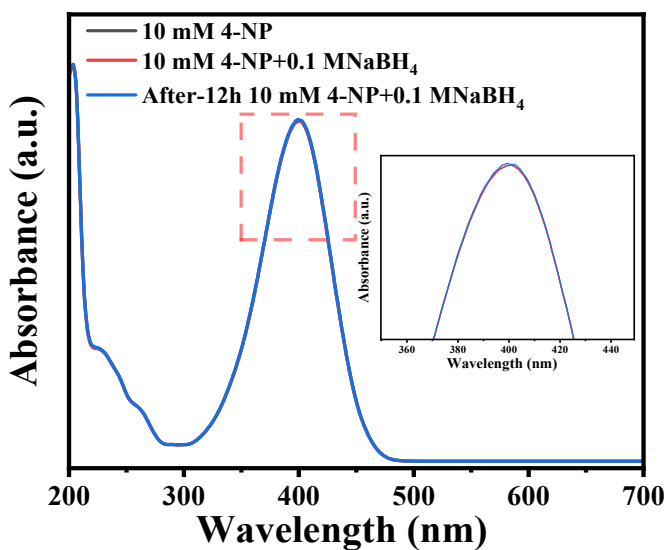


**Fig. S30.** UV-vis spectra of 1 M KOH aqueous solutions containing 10 mM 4-NP before and after the addition of  $\text{NaBH}_4$  (0.1 M), and the one after the addition of 0.1 M  $\text{NaBH}_4$  for 12 h.

**Note 2.** Because 4-AP is easily oxidized in the air,  $\text{NaBH}_4$  was used as an antioxidant during the reaction to accurately calibrate the yield of the products. Indeed, in the absence of electrical energy input, 4-NP undergoes an almost negligible conversion within 12 hours despite the presence of  $\text{NaBH}_4$ .

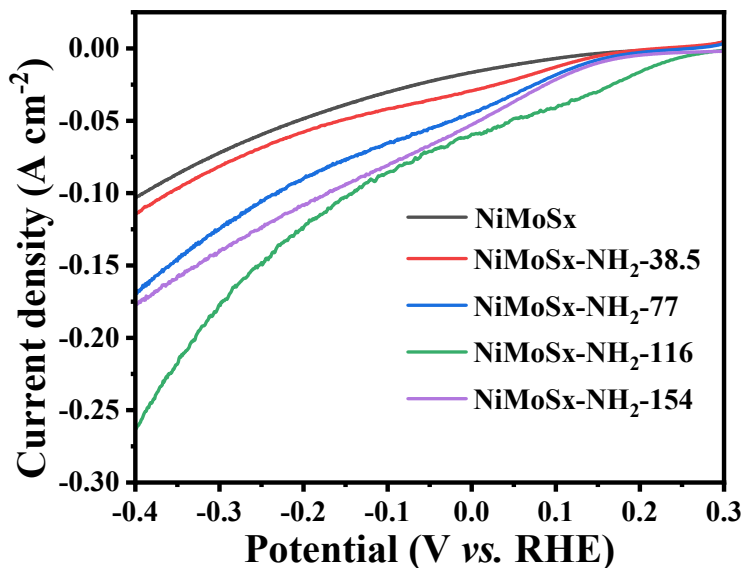


**Fig. S31.** LSV curves in 1 M KOH aqueous solution with 10 mM 4-NP of  $\text{NiMoSx-NH}_2\text{-}x$  series ( $x$  is the amount of ammonia).

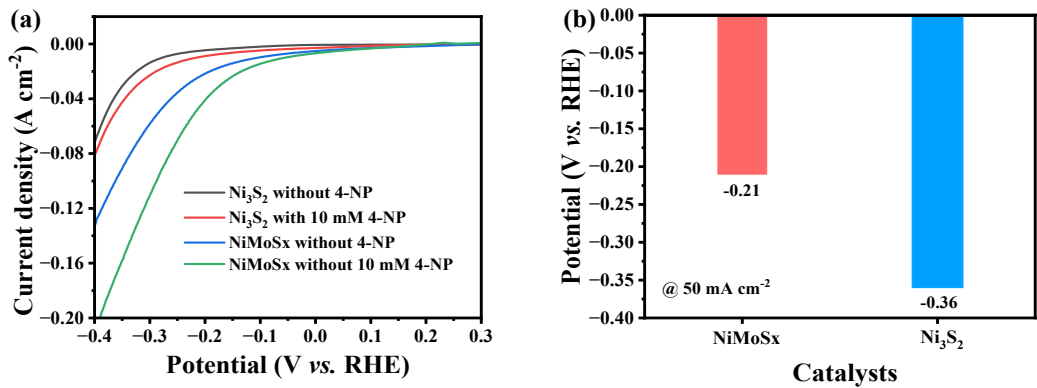


**Fig. S32.** (a) LSV curves, (b) potentials required at  $50 \text{ mA cm}^{-2}$  in 1.0 M KOH aqueous solution with 10 mM 4-NP of  $\text{Ni}_3\text{S}_2$  and NiMoSx.

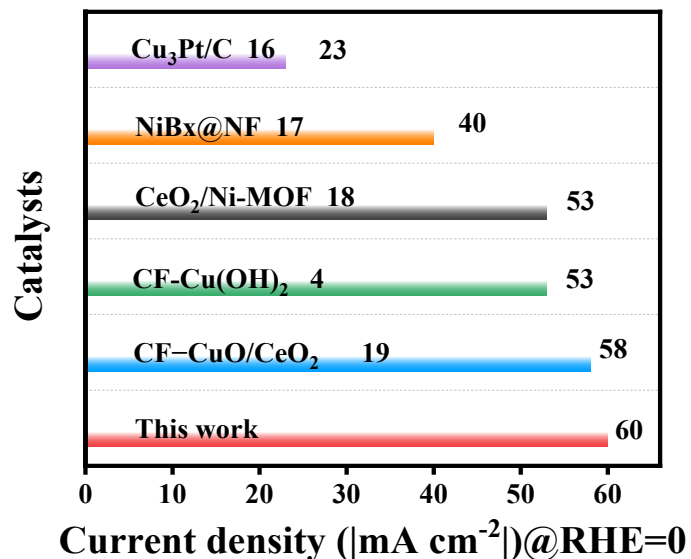


**Fig. S33.** Comparison of the performance of NiMoSx-NH<sub>2</sub> with those of previously reported electrocatalysts for hydrogenation of nitro compounds.<sup>[4,13]</sup>

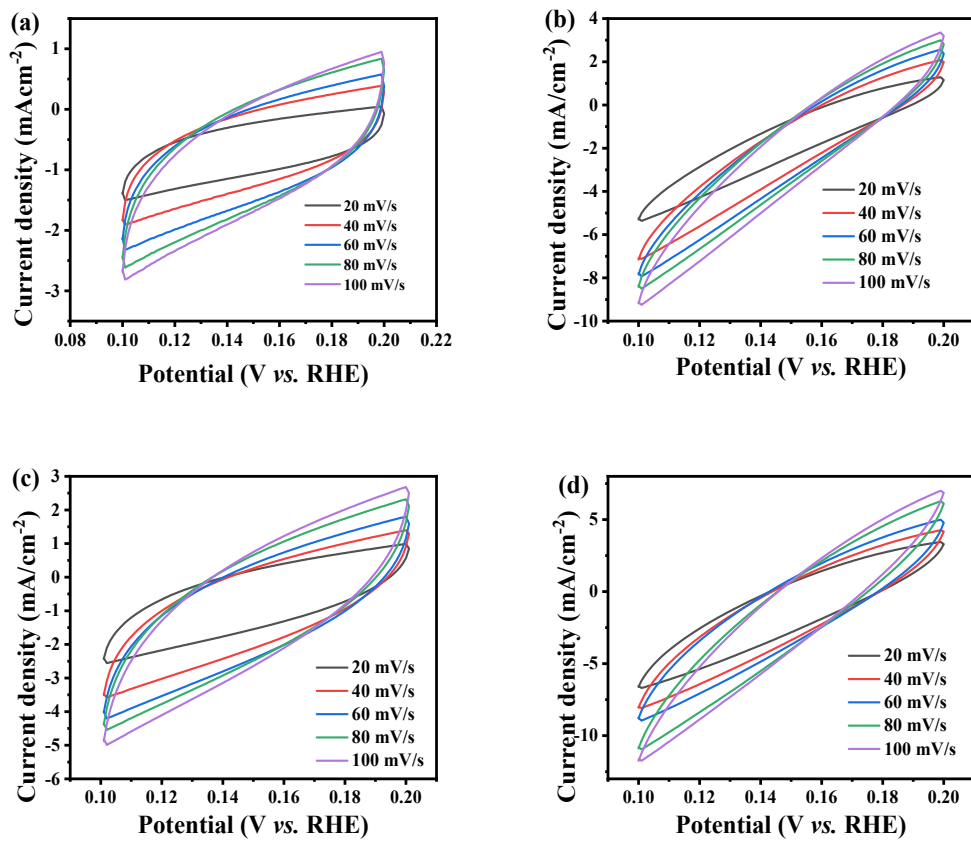


**Fig. S34.** CV curves of NiMoSx and NiMoSx-NH<sub>2</sub> in 1 M KOH without (a, c) or with (b, d) 10 mM 4-NP with the scan rate ranging from  $20 \text{ mVs}^{-1}$  to  $100 \text{ mVs}^{-1}$ .

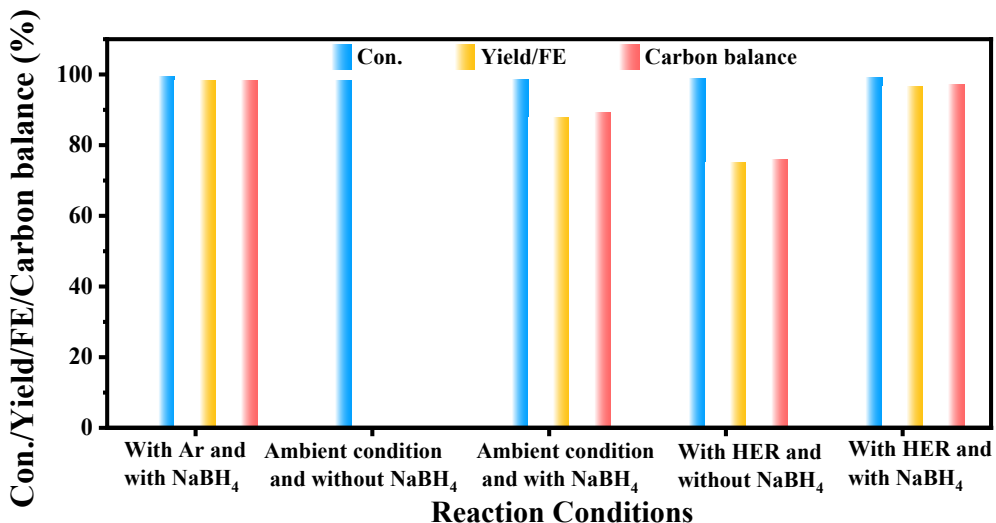


**Fig. S35.** Electrocatalytic 4-NP hydrogenation catalyzed by NiMoSx-NH<sub>2</sub> under different conditions. With Ar and with NaBH<sub>4</sub>: the reaction was carried out by using NaBH<sub>4</sub> as the antioxidant agent under the Ar atmosphere. Ambient condition and without NaBH<sub>4</sub>: the reaction was carried out in the absence of NaBH<sub>4</sub> under an ambient atmosphere. Ambient condition and with NaBH<sub>4</sub>: the reaction was carried out by using NaBH<sub>4</sub> as the antioxidant agent under an ambient atmosphere. With HER and without NaBH<sub>4</sub>: the reaction was firstly carried out HER for 1 h in the absence of NaBH<sub>4</sub>, and then 4-NP was added for the happening of 4-NP reduction in the presence of in situ formed H<sub>2</sub>. With HER and with NaBH<sub>4</sub>: the reaction was firstly carried out HER for 1 h in the presence of NaBH<sub>4</sub>, and then 4-NP was added for the happening of 4-NP reduction in the co-presence of NaBH<sub>4</sub> and in situ formed H<sub>2</sub>.

**Note 3.** Under argon gas atmosphere protection and with NaBH<sub>4</sub> as an antioxidant, the conversion of 4-AP was up to 99.4% after the reaction, and the yield and Faradaic efficiency of 4-AP exceeded 98%. Under ambient condition, no 4-AP was produced due to the oxidation of the hydrogenation product to form a quinone product with the electrolyte showing a dark brown color. When NaBH<sub>4</sub> was added as an antioxidant, the yield and Faradaic efficiency of 4-AP were enhanced to 87.9% and 89.2%. The yield of 4-AP was 75.1% with H<sub>2</sub> from HER and without NaBH<sub>4</sub>, which was due to the oxidation of the product by the oxygen dissolved in the electrolyte or in the air during

the test. The results obtained with H<sub>2</sub> produced by HER and the addition of NaBH<sub>4</sub> as an antioxidant were almost consistent with argon gas atmosphere protection in the presence of NaBH<sub>4</sub>, achieving 4-NP conversion of 99.3%, 4-AP yield of 96.5%, and 4-AP FE of 97.2%. Based on this, we performed the electrocatalytic hydrogenation reaction with NaBH<sub>4</sub> as an antioxidant and sealed in an argon gas atmosphere.

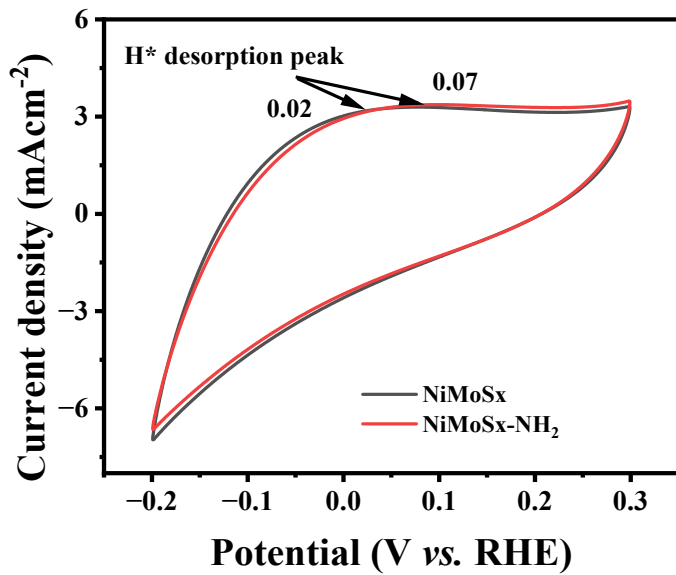


**Fig. S36.** CV curves of NiMoSx and NiMoSx-NH<sub>2</sub> in 1 M KOH with a scan rate of  $100 \text{ mVs}^{-1}$ .

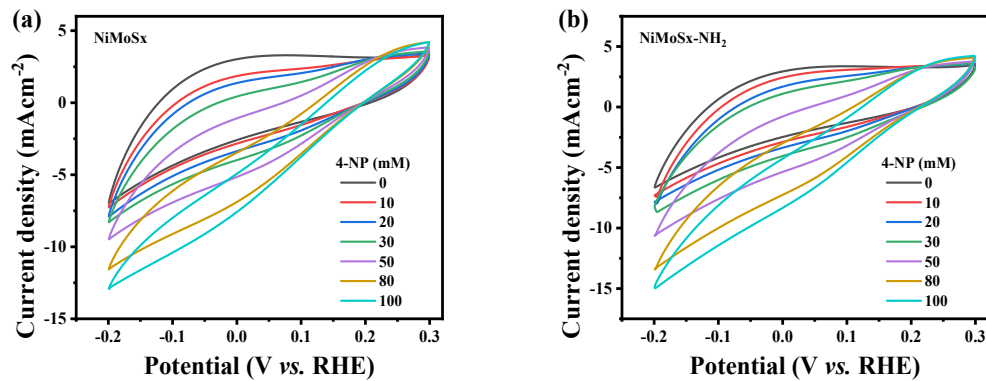


**Fig. S37.** CV curves of (a) NiMoSx and (b) NiMoSx-NH<sub>2</sub> in 1 M KOH containing 4-NP with different concentrations.

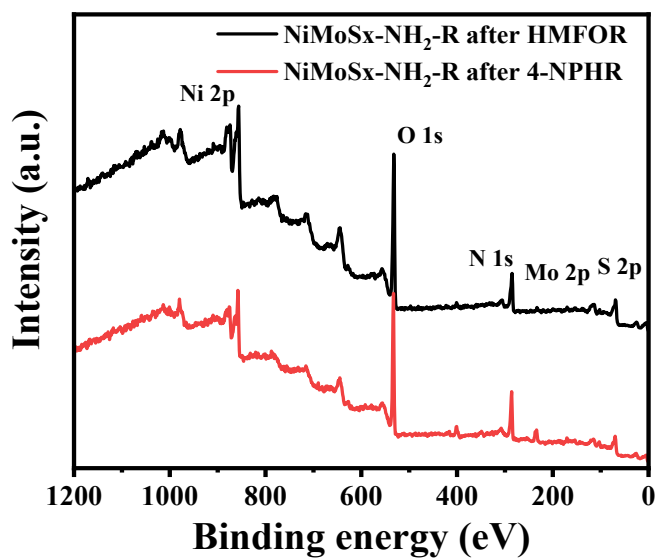


**Fig. S38.** Survey scan XPS spectra of spent NiMoSx-NH<sub>2</sub> recovered respectively after HMFOR and 4-NPHR.

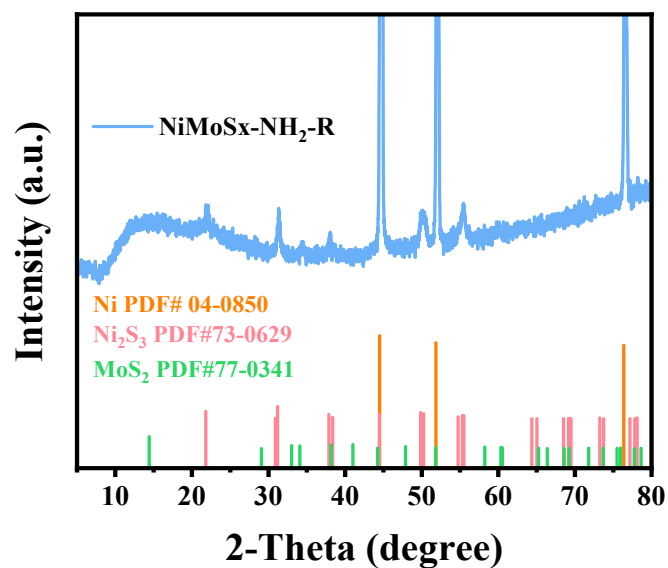


**Fig. S39.** XRD patterns of spent NiMoSx-NH<sub>2</sub>-R recovered after HMFOR.

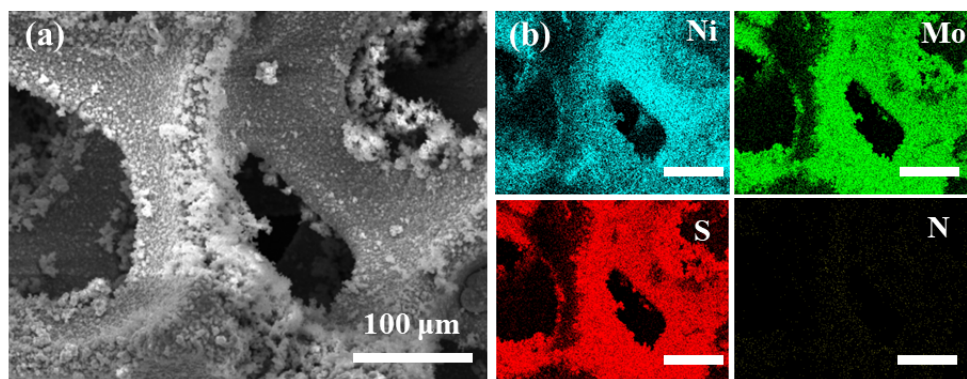


**Fig. S40.** (a) SEM image and (b) EDS elemental mapping profiles with Ni, Mo, S, and N distribution of spent NiMoSx-NH<sub>2</sub>-R recovered after HMFOR.

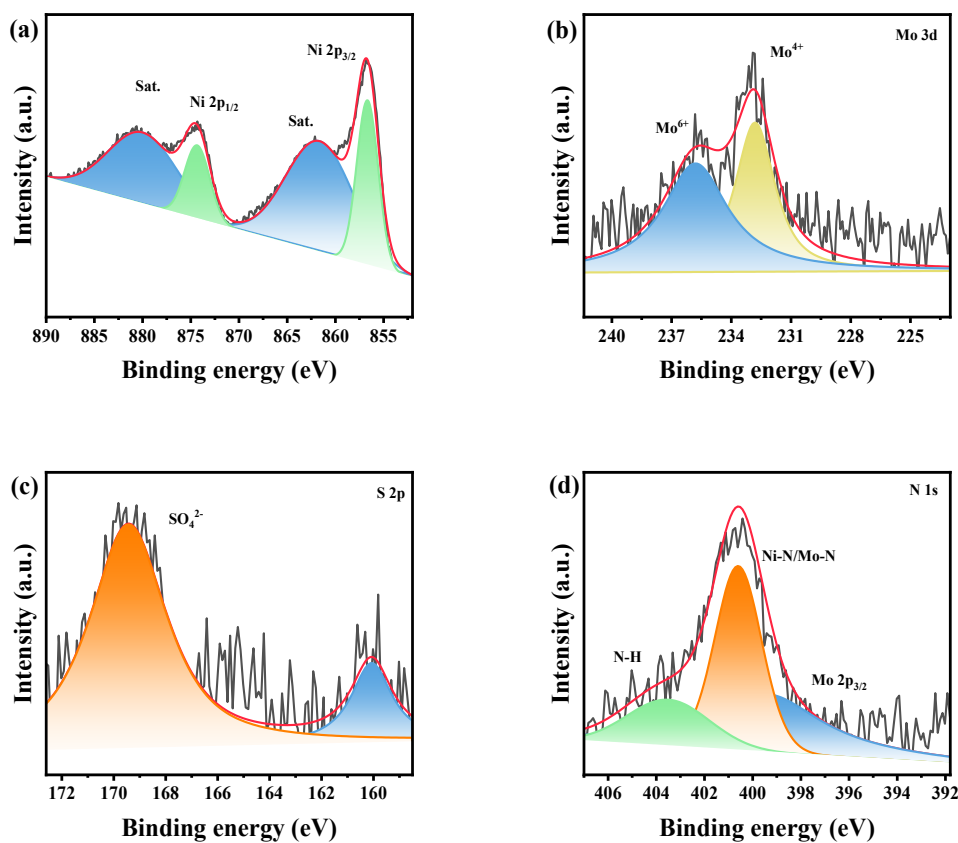


**Fig. S41.** High-resolution (a) Ni 2p, (b) Mo 3d, (c) S 2p, and (d) N 1s XPS spectra of spent NiMoSx-NH<sub>2</sub>-R recovered after HMFOR.

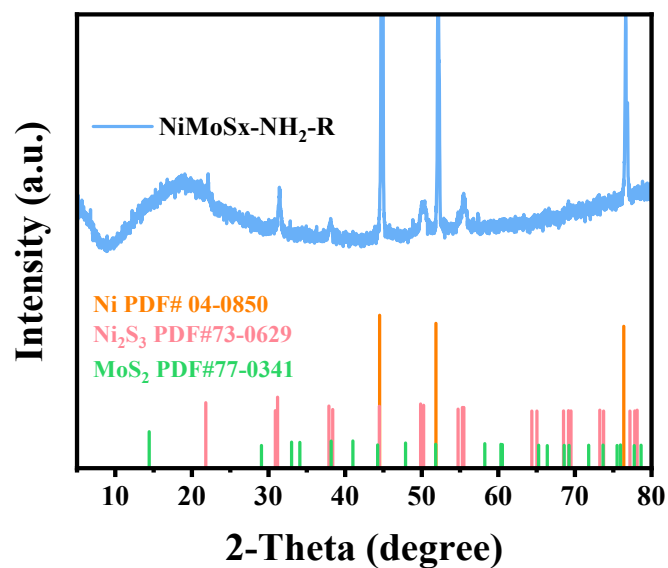


**Fig. S42.** XRD patterns of spent NiMoSx-NH<sub>2</sub>-R recovered after 4-NPHR.

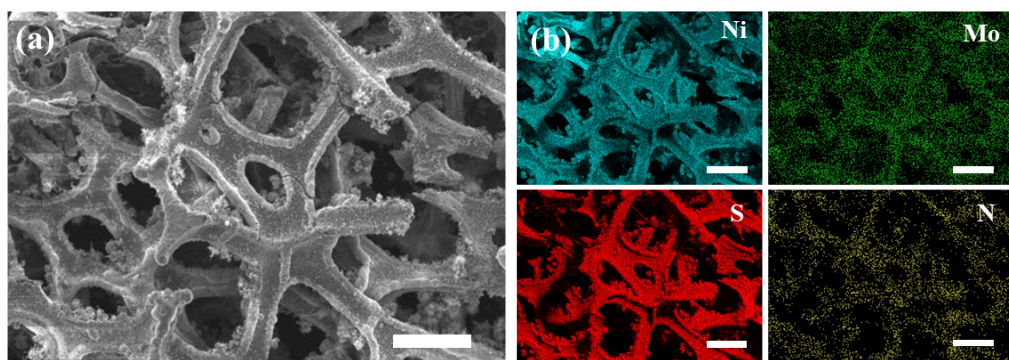


**Fig. S43.** (a) SEM image and (b) EDS elemental mapping profiles with Ni, Mo, S, and N distribution of spent NiMoSx-NH<sub>2</sub>-R recovered after 4-NPHR.

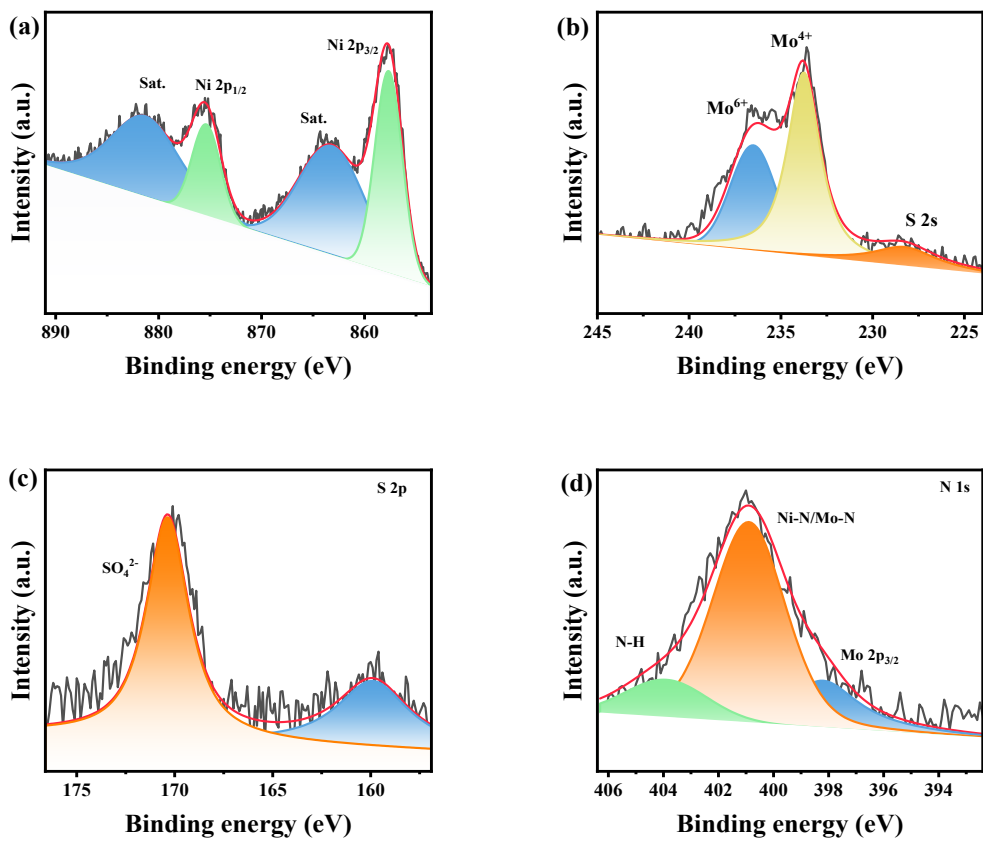


**Fig. S44.** High-resolution (a) Ni 2p, (b) Mo 3d, (c) S 2p, and (d) N 1s XPS spectra of spent NiMoSx-NH<sub>2</sub>-R recovered after 4-NPHR.

**Table S1.** Performance of electrocatalytic HMF oxidation

Catalysts	Potential (V vs. RHE)			Conv. (%)	Yield (%)	FE (%)	Refs.
	<i>j</i> <sub>10</sub>	<i>j</i> <sub>100</sub>	<i>j</i> <sub>200</sub>				
Pt/Ni(OH) <sub>2</sub>	1.39	-	-	100	96	98.7	[1]
NiCo <sub>2</sub> O <sub>4</sub>	1.47	-	-	99.6	90.4	87.5	[2]
NiCoFe-LDHs	1.52	1.76	-	96	85	90	[3]
CF-Cu(OH) <sub>2</sub>	1.44	1.81	1.96	100	98.7	98.7	[4]
Co <sub>9</sub> S <sub>8</sub> Ni <sub>3</sub> S <sub>2</sub> @NSOC/NF	1.33	1.35	1.52	100	98.8	98.6	[5]
CoNiP-NIE	1.25	1.64	1.71	-	95	87.2	[6]
Ni(OH) <sub>2</sub> /NF	1.31	1.44	1.84	100	>99	>99	[7]
FeP-NiMoP <sub>2</sub> /FNF	1.33	1.36	1.39	100	99.2	99	[8]
CoNiFe-MOFs/NF	1.31	1.35	1.56	100	99.76	>99	[9]
NF@Co <sub>3</sub> O <sub>4</sub> /CeO <sub>2</sub> <sup>b</sup>	1.33	1.52	-	98	94.5	97.8	[10]
Vo-Co <sub>3</sub> O <sub>4</sub> <sup>b</sup>	1.35	1.53	-	96.7	91.9	95	[11]
<b>NiMoSx-NH<sub>2</sub></b>	<b>1.29</b>	<b>1.39</b>	<b>1.49</b>	<b>100</b>	<b>&gt;99</b>	<b>&gt;99</b>	<b>This work</b>

<sup>a</sup>1 M KOH with 10 mM HMF, <sup>b</sup>1 M KOH with 50 mM HMF.

**Table S2.** Performance of electrocatalytic 4-NP hydrogenation<sup>a</sup>

Catalysts	Current density <i>@RHE=0</i>	Conv. (%)	Yield (%)	FE (%)	Refs.
CF-Cu(OH) <sub>2</sub>	53	100	96.8	96.8	[4]
Cu <sub>3</sub> Pt/C <sup>b</sup>	20	100	~99	~99	[13a]
NiBx@NF	40	≥99	≥99	≥99	[13b]
CeO <sub>2</sub> /Ni-MOF <sup>c</sup>	53	97.6	97.6	99.9	[13c]
CF-CuO/CeO <sub>2</sub>	58	99.5	98.6	90.4	[13d]
<b>NiMoSx-NH<sub>2</sub></b>	<b>60</b>	<b>99.7</b>	<b>99.6</b>	<b>99.6</b>	<b>This work</b>

<sup>a</sup>10 mM 4-NP in 1 M KOH, <sup>b</sup>5 mM Ph-NO<sub>2</sub> in 1 M KOH, <sup>c</sup>25 mM 4-NP in 1 M Na<sub>2</sub>SO<sub>4</sub>.

**Table S3.** Performance of paired electrocatalytic anodic oxidation coupled cathodic reduction reaction<sup>a</sup>

Catalysts	Couple reaction	Anode products/ FE (%)	Cathode products/ FE (%)	Current efficiency (%) <sup>b</sup>	Onset potential (V) @ 10mAcm <sup>-2</sup>	Refs.
FeP- MoP/FF  FeP- NiMoP <sub>2</sub> /FNF	HMFOR  4- NBARR	FDCA/99.2	4-ABA/98.6	197.8	1.13	[8]
NiBx/NiOx  NiBx	HMFOR  4-NPRR	FDCA/>99	4-AP/>99	>198	1.15	[13b]
PdO  PdOx/ZIF-8	HMFOR  CO <sub>2</sub> RR	MA/20, FA /63.4	CO/97	181.3	1.06	[14]
CuSn-4  CuSn-4	MOR  CO <sub>2</sub> RR	FA/99.1	FA/93.2	190	1.54	[15]
VN  Pd/VN	HMFOR  HMFRR	FDCA/84	DHMTHF/86	170	1.05	[16]
NiO(OH)ED  α- NiS	HMFOR  CO <sub>2</sub> RR	FDCA/96	CO/60	156	2.05	[17]
Ni(OH) <sub>2</sub>   Bi-MOF	HMFOR  CO <sub>2</sub> RR	FDCA/75	FA/95.6	170.6	1.2	[18]
Px-CoMoO <sub>4-x</sub>   Px- CoMoO <sub>4-x</sub>	LIOR  2-FARR	Ph-COOH/57 Ph-OH/48 Ph-OH/11	2-MF/83.9	183.9	1.36	[19]
NiCo-NF-ET  Ni- SAs@FNC	MOR  CO <sub>2</sub> RR	FA/>99	CO/>86	185	1.94	[20]
Ni(OH) <sub>2</sub>   NiCo@ N-CNTs	HMFOR  4-NPRR	FDCA/>99	AB/97.6	>196.6	1.2	[21]
TiO <sub>2</sub> -Al <sup>3+</sup>   Au/NF	OXH  EGO	GA/>99	GA/86	186	0.89	[22]
<b>NiMoSx-NH<sub>2</sub>   NiMoSx-NH<sub>2</sub></b>	<b>HMFOR  4-NPRR</b>	<b>FDCA/99.8</b>	<b>4-AP/97.8</b>	<b>197.6</b>	<b>0.89</b>	<b>This work</b>

<sup>a</sup>HMFOR: HMF oxide reaction, MOR: methanol oxide reaction, LIOR: lignin oxide reaction, 4-NBARR:4-nitrobenzyl alcohol reduction reaction, CO<sub>2</sub>RR: carbon dioxide reduction reaction, HMFRR: HMF reduction reaction, 4-NPRR:4-nitrophenol reduction reaction, 4-NPRR: nitrophenol reduction reaction, 2-FARR: 2-furaldehyde reduction reaction. OXH: oxalic acid electrocatalytic hydrogenation, EGO: ethylene glycol oxidation reaction. <sup>b</sup>Current efficiency: the sum of the Faraday efficiency of the anode and cathode.

## Reference:

- [1] B. Zhou, Y. Li, Y. Zou, W. Chen, W. Zhou, M. Song, Y. Wu, Y. Lu, J. Liu, Y. Wang, S. Wang, *Angew. Chem. Int. Ed.* **2021**, *60*, 22908-22914.
- [2] M. J. Kang, H. Park, J. Jegal, S. Y. Hwang, Y. S. Kang, H. G. Cha, *Appl. Catal., B.* **2019**, *242*, 85-91.
- [3] M. Zhang, Y. Liu, B. Liu, Z. Chen, H. Xu, K. Yan, *ACS Catal.* **2020**, *10*, 5179-5189.
- [4] X. Pang, H. Bai, H. Zhao, W. Fan, W. Shi, *ACS Catal.* **2022**, *12*, 1545-1557.
- [5] Y. Zhang, Z. Xue, X. Zhao, B. Zhang, T. Mu, *Green Chem.* **2022**, *24*, 1721-1731.
- [6] Y. Song, W. Xie, Y. Song, H. Li, S. Li, S. Jiang, J. Y. Lee, M. Shao, *Appl. Catal., B.* **2022**, *312*, 121400.
- [7] J. Zhang, W. Gong, H. Yin, D. Wang, Y. Zhang, H. Zhang, G. Wang, H. Zhao, *ChemSusChem.* **2021**, *14*, 2935-2942.
- [8] G. Yang, Y. Jiao, H. Yan, Y. Xie, C. Tian, A. Wu, Y. Wang, H. Fu, *Nat. Commun.* **2022**, *13*, 3125.
- [9] X.-J. Bai, W.-X. He, X.-Y. Lu, Y. Fu, W. Qi, *J. Mater. Chem. A.* **2021**, *9*, 14270-14275.
- [10] G. Zhao, G. Hai, P. Zhou, Z. Liu, Y. Zhang, B. Peng, W. Xia, X. Huang, G. Wang, *Adv. Funct. Mater.* **2023**, *33*, 2213170.
- [11] Y. Lu, T. Liu, C. L. Dong, C. Yang, L. Zhou, Y. C. Huang, Y. Li, B. Zhou, Y. Zou, S. Wang, *Adv. Mater.* **2022**, *34*, e2107185.
- [12] a) L. Xu, Z. Huang, M. Yang, J. Wu, W. Chen, Y. Wu, Y. Pan, Y. Lu, Y. Zou, S. Wang, *Angew. Chem. Int. Ed.* **2022**, *61*, e202210123; b) D. Chen, Y. Ding, X. Cao, L. Wang, H. Lee, G. Lin, W. Li, G. Ding, L. Sun, *Angew. Chem. Int. Ed.* **2023**, *62*, e202309478; c) J. Wu, J. Chen, T. Yu, Z. Zhai, Y. Zhu, X. Wu, S. Yin, *ACS Catal.* **2023**, *13*, 13257-13266; d) C. Liu, X. R. Shi, K. Yue, P. Wang, K. Zhan, X. Wang, B. Y. Xia, Y. Yan, *Adv. Mater.* **2023**, *35*, e2211177.
- [13] a) M. Jin, Y. Liu, X. Zhang, J. Wang, S. Zhang, G. Wang, Y. Zhang, H. Yin, H. Zhang, H. Zhao, *Appl. Catal., B.* **2021**, *298*, 120545; b) P. Zhang, X. Sheng, X. Chen, Z. Fang, J. Jiang, M. Wang, F. Li, L. Fan, Y. Ren, B. Zhang, B. J. J. Timmer, M. S. G. Ahlquist, L. Sun, *Angew. Chem. Int. Ed.* **2019**, *58*, 9155-9159; c) H. Zhao, X. Pang, Y. Huang, C. Ma, H. Bai, W. Fan, *Inorg. Chem.* **2022**, *61*, 19806-19816; d) X. Pang, H. Zhao, Y. Huang, Y. Liu, H. Bai, W. Fan, W. Shi, *Inorg. Chem.* **2022**, *61*, 8940-8954.
- [14] J. Bi, Q. Zhu, W. Guo, P. Li, S. Jia, J. Liu, J. Ma, J. Zhang, Z. Liu, B. Han, *ACS Sustainable Chem. Eng.* **2022**, *10*, 8043-8050.
- [15] Y. Li, C.-Z. Huo, H.-J. Wang, Z.-X. Ye, P.-P. Luo, X.-X. Cao, T.-B. Lu, *Nano Energy.* **2022**, *98*, 107277.
- [16] S. Li, X. Sun, Z. Yao, X. Zhong, Y. Cao, Y. Liang, Z. Wei, S. Deng, G. Zhuang, X. Li, J. Wang, *Adv. Funct. Mater.* **2019**, *29*, 1904780.
- [17] A. Kundu, B. Kumar, A. Rajput, B. Chakraborty, *ACS Appl. Mater. Interfaces.* **2023**, *15*, 8010-8021.
- [18] Z. W. Yang, J. M. Chen, Z. L. Liang, W. J. Xie, B. Zhao, L. N. He, *ChemCatChem.* **2022**, *15*, e202201321.
- [19] Y. Qi, B. Liu, X. Qiu, X. Zeng, Z. Luo, W. Wu, Y. Liu, L. Chen, X. Zu, H. Dong, X. Lin, Y. Qin, *Adv. Mater.* **2023**, e2208284.
- [20] J. Tian, C. Cao, D.-D. Ma, S.-G. Han, Y. He, X.-T. Wu, Q.-L. Zhu, *Small Struct.* **2021**, *3*, 2100134.
- [21] W. Gong, X. Mao, J. Zhang, Y. Lin, H. Zhang, A. Du, Y. Xiong, H. Zhao, *ACS Nano.* **2023**, *17*, 3984-3995.
- [22] L. Hao, Q. Ren, J. Yang, L. Luo, Y. Ren, X. Guo, H. Zhou, M. Xu, X. Kong, Z. Li, M. Shao, *ACS Appl. Mater. Interfaces.* **2023**, *15*, 13176-13185.